Res Chem Intermed (2017) 43:5091–5102
DOI 10.1007/s11164-017-3050-0

Facile synthesis of Fe_2O_3/Cu_2O nanocomposite and its visible light photocatalytic activity for the degradation of cationic dyes

Sandeep Kumar Lakhera[1] · R. Venkataramana[1] · Aakash Watts[2] · Masakazu Anpo[3] · Bernaurdshaw Neppolian[4]

Received: 18 April 2017 / Accepted: 2 June 2017 / Published online: 17 July 2017

Abstract Iron oxide-loaded Cu_2O photocatalysts were prepared by a facile hydrothermal method. The binary mixed metal oxide photocatalyst was characterized by XRD, FE-SEM, FTIR, UV–Vis-DRS, particle size and zeta potential measurements. XRD analysis showed that Fe_2O_3/Cu_2O catalysts were phase pure and highly crystalline in nature. FE-SEM images revealed the formation of nanospherical Fe_2O_3 over the Cu_2O surface during hydrothermal reaction. From UV–Vis diffuse reflectance spectroscopy studies, the optical band gap of the Fe_2O_3/Cu_2O photocatalyst was found to be slightly red-shifted to 1.85 eV, after loading of Fe_2O_3. The zeta potential analysis revealed that the surface of the Fe_2O_3/Cu_2O photocatalyst was negatively charged in neutral solution. The loading of *n*-type Fe_2O_3 on *p*-type Cu_2O augments the charge carrier separation at the interface, which was evident from the enhanced photodegradation of organic pollutants (Methylene blue and Rhodamine B dyes) under visible light irradiation.

Keywords Photocatalyst · Cu_2O · Fe_2O_3 · *p–n* junction · Nanocomposite

Special Issue of the 1st International Symposium on Photocatalysis at Fuzhou University.

✉ Bernaurdshaw Neppolian
neppolian.b@res.srmuniv.ac.in

[1] Department of Physics and Nanotechnology, SRM University, Kattankulathur, Chennai, Tamil Nadu 603203, India

[2] Department of Chemical Engineering, SRM University, Kattankulathur, Chennai, Tamil Nadu 603203, India

[3] State Key Laboratory of Photocatalysis on Energy and Environment, Fuzhou University, 2 Xueyuan Road, University Town, Fuzhou 350116, Fujian, People's Republic of China

[4] SRM Research Institute, SRM University, Kattankulathur, Chennai, Tamil Nadu 603203, India

Introduction

Harvesting energy from sunlight by mimicking the photosynthesis process is one of the promising methods to produce a green and sustainable solution for environmental remediation [1]. Semiconductor-based visible light photocatalysts are indispensable for the development of such technologies due to their effective utilization of naturally abundant solar energy and their recyclability [2]. One of the major issues associated with metal oxides is the fast recombination probability of the charge carriers, which can be circumvented by designing a hetero-, homo- or Schottky junction between the metal oxides. The mixed metal oxides provide a superior charge transfer efficiency and activity compared to a single-metal oxide semiconductor [3–6]. Extensively used semiconductors such as TiO_2-, SnO_2-, and ZrO_2-based mixed-metal oxides, owing to their large band gap respond only to UV radiation, which accounts for only 3–5% of the natural sunlight [7, 8]. Therefore, this limits the efficiency and commercial viability of the catalysts to work under visible light irradiation. Visible light, on the other hand, constitutes nearly 43% of the solar spectrum [9].

In recent years, the search for a visible light-driven semiconducting material has led to the development of non-titania-based semiconducting photocatalysts [10, 11]. Among the various visible light photocatalysts, Cu_2O is an earth-abundant *p*-type photocatalyst with a direct band gap in the visible range (2.0–2.2 eV) [12–15]. However, Cu_2O suffers from photo-instability and photo-corrosion and can easily become deactivated under solar irradiation [16]. Hematite (Fe_2O_3), on the other hand, is very stable *n*-type semiconductor under ambient conditions [17], having a band gap of 2.0–2.2 eV. The valence band edge of Fe_2O_3 is more negative than the redox potential for water oxidation, which makes it an excellent catalyst for photodegradation of environmental pollutants [18]. However, its photocatalytic activity is hindered by its hort hole diffusion length (<10 nm) and a very short electron–hole recombination time ($\sim$10 ps) [19–24]. Since both the oxides are low-cost and non-toxic and harvest sunlight in the visible range, a Fe_2O_3-loaded Cu_2O nanocomposite was prepared by a facile and environmentally friendly method and the *p–n* heterojunction nanocomposite was used for the effective degradation of organic pollutants, namely, Rhodamine B (RhB) and Methylene blue (MB).

Materials and methods

Materials and characterization

The precursor salts Cu_2O [$Cu(CH_3COO)_2.H_2O$] and Fe_2O_3 [$Fe(NO_3)_3.9H_2O$] were purchased from Sigma-Aldrich, India, and SRL Chemicals, India, respectively. The entire chemicals were used without any further purification.

The crystallinity and phase purity of the nanocomposite were analyzed in the range of 4°–90° by X-ray diffraction (PANaltical X'pert powder diffractometer) using Cu Kα radiation ($\lambda = 1.5406$ Å). Field emission scanning electron

microscopy (FEI Quanta FEG 200) was used to examine the surface morphology. UV-2600 spectrophotometer (Shimadzu) was used to recorded the diffuse reflectance spectra (DRS) in the range of 400–900 nm. Fourier transform infrared spectroscopy (FTIR) was recorded on a Perkin Elmer instrument (USA).

Synthesis of FeCu photocatalyst

The photocatalyst was prepared by dissolving 0.233 M copper acetate monohydrate and a certain amount of Iron nitrate nonahydrate in 50 ml deionized water, followed by a 5-min ultrasonication. 20 ml of NH_4OH was added to the solution under stirring for 1 h. The reddish suspension was transferred into a 100-ml Teflon-lined autoclave and kept at 180 °C for 12 h. After cooling, the reddish product was collected by centrifugation, washed with deionized water several times and dried at 60 °C overnight. The Fe_2O_3/Cu_2O sample was named as FeCu. Bare Cu_2O and bare Fe_2O_3 were also prepared by the similar method.

Photocatalytic activity

To measure the photocatalytic degradation ability of the catalysts, RhB and MB, were used as model pollutants, and 30 mg of the photocatalyst was dispersed in 30 ml of aqueous dye solution (10 mg/L) and stirred under dark condition for 30 min to achieve dsorption–desorption equilibrium. After the dark condition, the solution was irradiated with visible light using a Xenon lamp with cut-off filter ($\lambda > 400$ nm) (250 W; Oriel Instruments). At regular time intervals, 3 ml of an aliquot of the sample were collected, centrifuged and the dye samples were analyzed for % photodegradation by using the UV–visible spectrophotometer.

Results and discussion

Structural and morphological properties

The XRD pattern of Fe_2O_3/Cu_2O (FeCu) photocatalyst with jcpds data for Cu_2O and Fe_2O_3 is shown in Fig. 1. The diffraction peaks at $2\theta = 29.55$, 36.41, 42.29, 52.4, 61.34 and 73.53 are attributed to the (110), (111), (200), (211), (220) and (311) crystal planes of cubic (primitive) Cu_2O, respectively (JCPDS 05-0667). The intensity of the (111) plane indicates preferential growth of the Cu_2O crystals along the [111] direction [25]. The diffraction peaks observed at $2\theta = 33.15$ and 35.61 correspond to the (104) and (110) planes of rhombohedral Fe_2O_3, respectively (JCPDS 33-0664) [26].

Figure 2a, b shows the surface morphology of the FeCu photocatalyst. Figure 2a displays the cubic-shaped agglomerated Cu_2O with Fe_2O_3 nanospheres distributed all over its surface. During the growth process of the FeCu photocatalyst, Fe_2O_3 and Cu_2O grow into two different morphologies. Figure 2d shows the uniformly formed nanospheres of Fe_2O_3 after undergoing a hydrothermal reaction at 180 °C for 12 h without the Cu_2O precursor salt. Energy dispersive spectroscopy (EDS) analysis

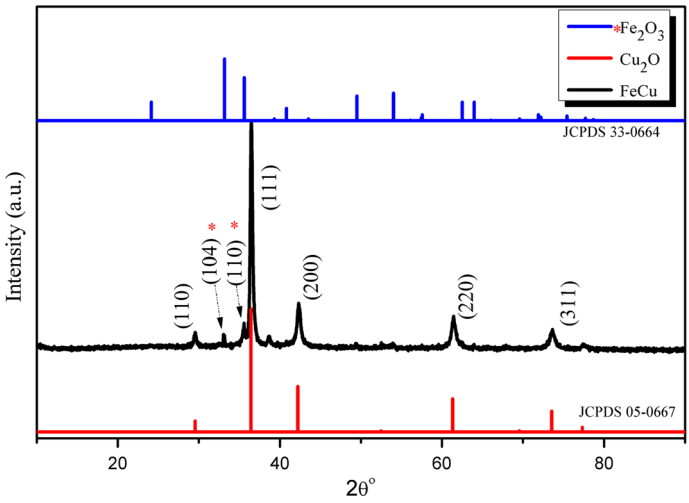

Fig. 1 XRD patterns of FeCu photocatalyst with JCPDS data for bare Cu_2O and Fe_2O_3

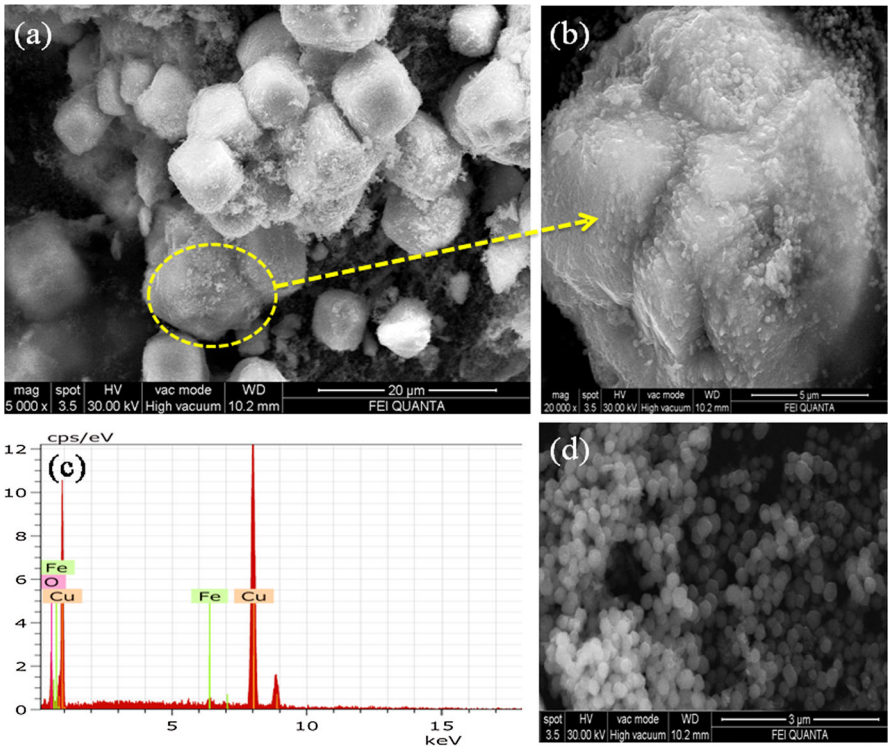

Fig. 2 FE-SEM images of **a**, **b** FeCu photocatalyst, **c** energy dispersive spectroscopy analysis of FeCu photocatalyst and **d** bare Fe_2O_3

confirmed the phase purity of the FeCu photocatalyst, as shown in Fig. 2c. Based on theoretical calculations, a certain amount of Iron nitrate nonahydrate was used in the synthesis of the nanocomposite; however, EDS analysis revealed that the amount of Fe_2O_3 formed in the final product was 1.5 wt% for the optimized sample. The excess amount of unreacted iron salt was filtered out during the washing process. Table 1 shows the elemental composition of the FeCu photocatalyst.

Figure 3 represents the FTIR spectrum of the Cu_2O, Fe_2O_3 and FeCu photocatalysts. The common strong peak observed in the photocatalysts at 3448 and 1635 cm^{-1} are assigned to O–H bond stretching and bending vibration modes, respectively [27]. The characteristic broad absorption peak centered at 622.97 cm^{-1} is due to the Infrared active mode of Cu_2O [28]. For bare Fe_2O_3, the absorption peaks at 553.52 and 474.46 represent the Fe^{3+}–O^{2-} bond stretching in the FeO_6 octahedron and Fe^{3+}–O^{2-} bond stretching in the FeO_4 tetrahedron, respectively [29]. The nanocomposite FeCu shows the presence of IR peaks corresponding to both the photocatalysts, Cu_2O and Fe_2O_3.

The average particle size distribution measurement of the FeCu photocatalyst was carried out using a Zetasizer Nano ZEN3690 (Malvern Instruments, UK). As shown in Fig. 4, the particle sizes are distributed in the range of 170–528 nm, and

Table 1 The elemental composition of FeCu photocatalyst determined from energy dispersive spectroscopy

Elements	Atomic number	Norm. C (wt%)	Atomic C (at%])	Error C (1Sigma)
Cu	29	82.18	55.29	1.75
Fe	26	1.53	1.17	0.11
O	8	16.29	43.54	3.46

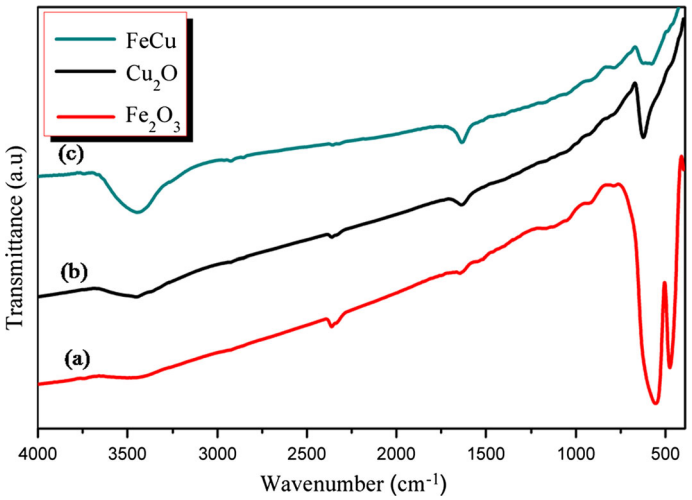

Fig. 3 FTIR spectra of **a** Fe_2O_3, **b** Cu_2O and **c** FeCu photocatalysts

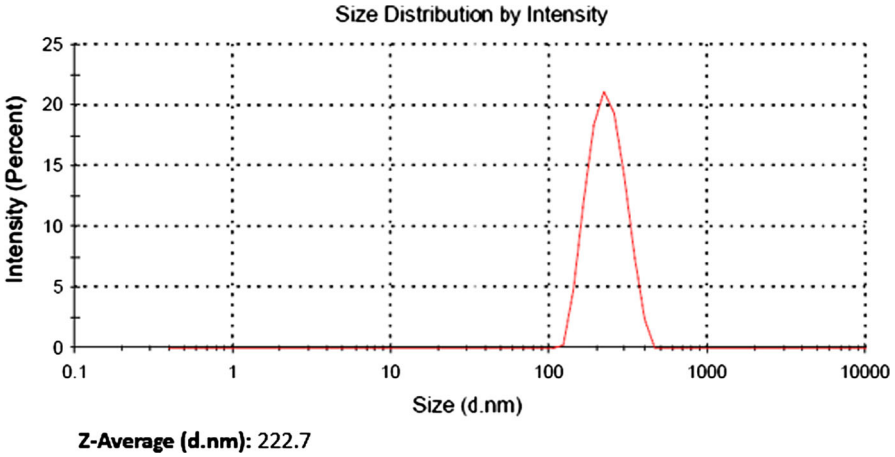

Fig. 4 Average particle size distribution of the FeCu photocatalyst

the average particle size is about 223 nm. The stability analysis of the FeCu particles in de-ionized water suspension was carried out by zeta potential measurement (Fig. 5). The surface charge on the metal oxides in aqueous solution appears due to the process of hydration, protonation, and deprotonation of the surface groups [30]. MB is a cationic dye and hardly absorbs on the Cu_2O surface due to its positive zeta potential; however, for the FeCu photocatalyst, the measured zeta potential was found to be −0.967 mV, indicating the presence of a negative charge on the surface of the FeCu photocatalyst [31]. The negative surface charge favors the adsorption of cationic dyes on the FeCu photocatalyst due to the increased electrostatic force of attraction. The surface conductivity of the FeCu photocatalyst was found to be 0.229 mS cm^{-1}.

DRS were used to investigate the light-harvesting nature of the FeCu photocatalyst. As shown in Fig. 6, the band gap energies of the Cu_2O, Fe_2O_3 and FeCu photocatalysts are in the visible region. The associated band gap values were calculated using the following Eq. [32]:

$$\alpha h\nu = A\left(h\nu - E_g\right)^{\eta}$$

where α, h, ν, A and E_g are the absorption coefficient, Plank's constant, frequency of light, proportionality constant and band gap energy, respectively. The variable η depends on the nature of the optical transition. The band gap energy of a direct band gap semiconductor can be estimated from Tauc plot of $\alpha h\nu$ versus $h\nu$ with $\eta = 0.5$. The optical absorption coefficient (α) can be obtained from the Kubelka–Munk function. The calculated band gaps of bare Fe_2O_3 and bare Cu_2O were found to be 1.96 and 1.88 eV, respectively; which are consistent with the literature [33, 34]. The observed small red-shift in the band gap value (1.85 eV) of the FeCu photocatalyst is possibly due to the formation of a p–n heterojunction between the p-type Cu_2O and the n-type Fe_2O_3 [35].

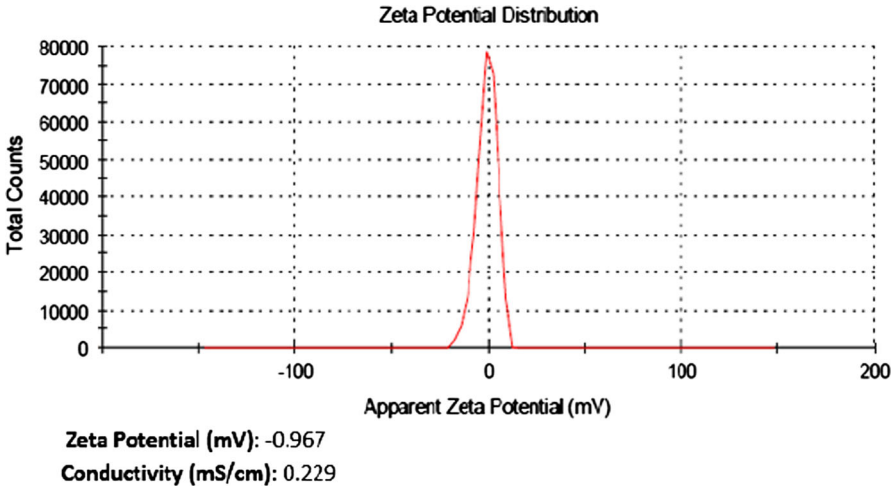

Fig. 5 Zeta potential of the FeCu photocatalyst measured in aqueous solution

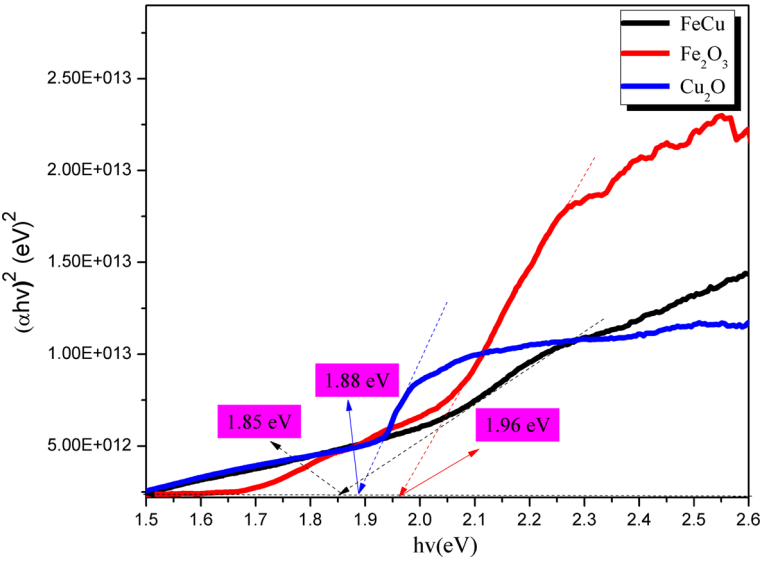

Fig. 6 Tauc plot for the band gap calculation of **a** Cu_2O, **b** Fe_2O_3 and **c** FeCu photocatalysts

The formation of a heterojunction and resulting charge separation activity of the FeCu photocatalyst was investigated by the photodegradation of RhB and MB dyes in aqueous solution under visible light irradiation. Figure 7a, b shows the temporal evolution of absorption spectra of the RhB and MB dyes, respectively. The characteristic absorption peaks of RhB at 554 nm and MB at 663 nm decreases with increasing the visible light irradiation time in the presence of the FeCu photocatalyst. Different amounts of Fe_2O_3-loaded Cu_2O were prepared and used

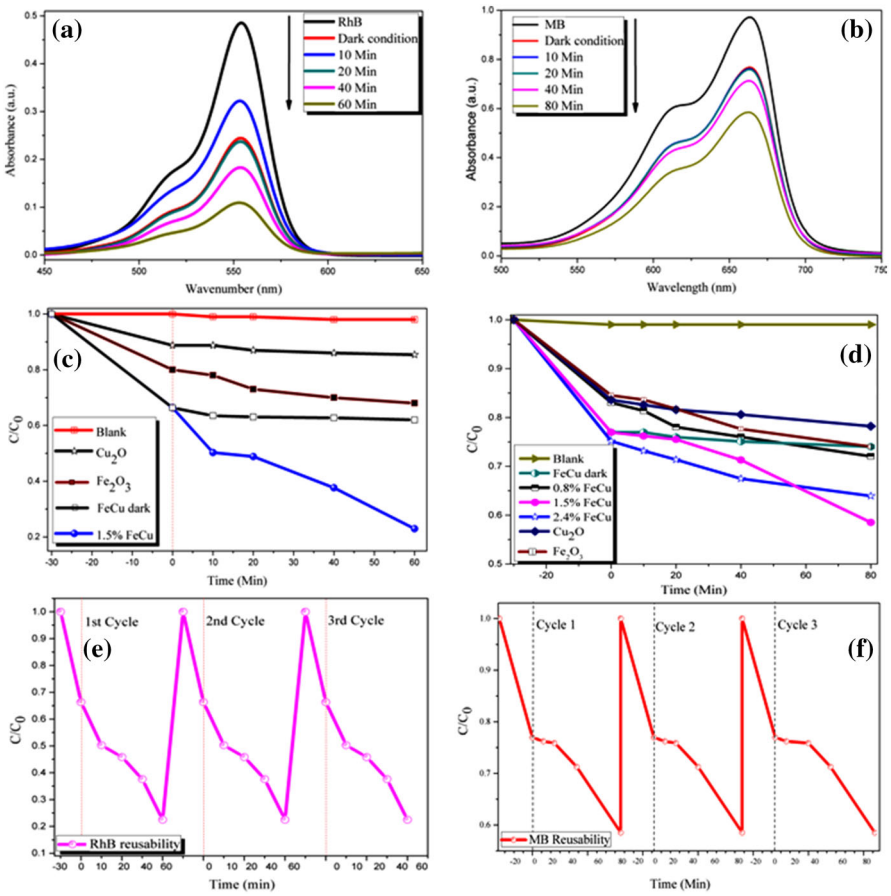

Fig. 7 **a**, **b** Visible light absorbance spectra depicting the change in the concentration of RhB and MB dyes as a function of time using FeCu photocatalyst; **c**, **d** rate of photocatalytic degradation of RhB and MB dyes as a function of time for Fe_2O_3, Cu_2O, FeCu catalysts and **e**, **f** reusability test of FeCu photocatalyst for RhB and MB dyes, respectively

for the photocatalytic dye degradation activity. It was found that 1.5 wt% loading of Fe_2O_3 on Cu_2O exhibited a superior performance compared to those of 0.8 and 2.4 wt% loading. Figure 7c, d displays the rate of the adsorption and photodegradation of RhB and MB dyes for Cu_2O, Fe_2O_3 and FeCu. The optimized photocatalyst (FeCu), due to its negative surface charge, was found to adsorb nearly 35 and 24% of the RhB and MB dyes, respectively, under dark stirring conditions. Under visible light irradiation, the FeCu photocatalyst effectively degraded nearly 43% of RhB dye in 60 min compared to 4 and 13% photodegradation exhibited by bare Cu_2O and Fe_2O_3, respectively. Similarly, 20% degradation of MB dye occurred in 80 min compared to 6 and 10% shown by bare Cu_2O and Fe_2O_3, respectively.

It can be clearly seen that 1.5 wt% Fe_2O_3-loaded Cu_2O photocatalyst is much more efficient than bare Cu_2O towards cationic dyes (RhB and MB) degradation.

Compared to bare Cu_2O, the FeCu photocatalyst enhances the degradation rate of RhB by 39% and of MB by 14% under visible light irradiation. To evaluate the stability and reusability of the FeCu photocatalyst, three additional cycles of dye (RhB and MB) degradation was performed with it. Figure 7e, f shows the good recyclability of the FeCu photocatalyst for three consecutive cycles. A slight decrease in activity for the third cycle of MB may be due to the loss of catalyst during recyclability. Total organic carbon analysis was performed to check the rate of mineralization of RhB and MB under visible light irradiation. As shown in Fig. 8, the % mineralization of RhB and MB with the FeCu photocatalyst was found to be nearly 30 and 10%, respectively. This result clearly indicates that both dyes degraded into carbon dioxide and water as final products.

Plausible photocatalytic mechanism of FeCu photocatalyst

To understand the photogenerated charge carrier separation mechanism between Fe_2O_3 and Cu_2O, the band edge positions of the FeCu photocatalyst were estimated. The position of the conduction band edge and the valence band edge according to the Mulliken electronegativity theory can be calculated as [36].

$$E_{CB} = \chi - E_e - 0.5\,E_g$$

$$E_{VB} = E_{CB} + E_g$$

where χ is the Mulliken electronegativity of the semiconductor, E_{CB} and E_{VB} are the conduction and valence band edge potential, respectively, E_g is the band gap of the semiconductor and E_e is the energy of free electrons on the hydrogen scale (4.5 eV). For Cu_2O and Fe_2O_3, the electronegativity values are reported to be 5.32 and 5.88 eV, respectively [37]. Based on the estimated band gap values of Cu_2O and

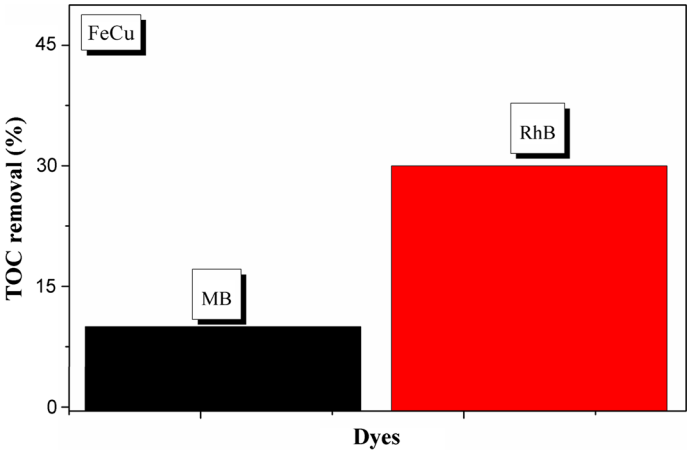

Fig. 8 Total organic carbon analyses of FeCu photocatalysts under visible light irradiation for RhB and MB dyes

Table 2 The electronegativity, band gap, conduction band (*CB*) edge and valence band (*VB*) edge potential of the catalysts on normalized hydrogen scale

Semiconductor	χ (eV)	E_g (eV)	E_{CB} (eV)	E_{VB} (eV)
Cu_2O	5.32	1.88	−0.12	1.76
Fe_2O_3	5.88	1.96	0.395	2.355

Fe_2O_3 from UV–Vis diffuse reflectance measurement, the conduction and valence band edges of the photocatalyst are set out in Table 2.

Figure 9 shows the band alignment of the FeCu photocatalyst. It can be seen that the conduction band edge of Cu_2O is negative and the conduction band edge of Fe_2O_3 is positive with respect to the hydrogen reduction potential on the normalized hydrogen scale. Similarly, the valence band edge of Fe_2O_3 is more positive than that of Cu_2O (Table 2). As Cu_2O is a *p*-type and Fe_2O_3 is an *n*-type semiconductor with different electronegativities and band edge positions, a *p*–*n* heterojunction forms at the interface in accordance with Anderson's model [38–42]. At the interface, an internal electric field will build up, directed from the Fe_2O_3 surface to the Cu_2O surface. When exposed to visible light irradiation ($\lambda > 400$ nm), the photogenerated electrons will move under the influence of an internal electric field from *p*-type Cu_2O to *n*-type Fe_2O_3, and the photogenerated holes will migrate from the valence bands of Fe_2O_3 to the valence band of Cu_2O. This effectively separates the photogenerated electron and holes; therefore enhancing the photocatalytic activity of FeCu photocatalysts.

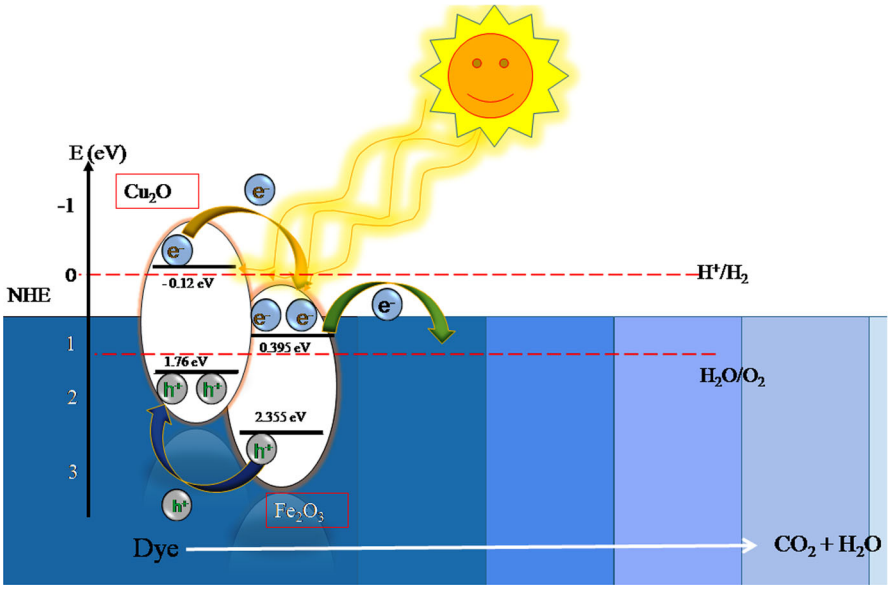

Fig. 9 Proposed photocatalytic degradation mechanism of FeCu photocatalyst under visible light irradiation

Conclusion

In summary, a visible light-driven Fe_2O_3/Cu_2O heterojunction photocatalyst was prepared by a facile hydrothermal method. The XRD pattern revealed that the photocatalyst was composed of rhombohedral Fe_2O_3 and primitive Cu_2O. FE-SEM analysis revealed that Fe_2O_3 transforms into nanospheres under the hydrothermal conditions and retains the nanospherical morphology in the FeCu nanocomposite. A slight red-shift in the band gap of Cu_2O was observed after loading of Fe_2O_3. The photocatalytic activity of Cu_2O under visible light irradiation for the degradation of cationic dyes (RhB and MB) significantly increased after addition of Fe_2O_3. This might be due to the formation of an effective heterojunction between Cu_2O particles and Fe_2O_3 nanospheres and also the presence of negative charges on the surface of the Fe_2O_3/Cu_2O photocatalyst, as revealed by zeta potential measurements in neutral solution. Furthermore, the photocatalyst can be recycled several times without any significant loss of photocatalytic activity. The simple preparation method, earth abundance, and visible light photoactivity of such nanocomposites can be further improved by controlling the morphologies and designing the semiconductor–semiconductor–carbon junctions, which would further increase its utilization in wastewater remediation.

Acknowledgement We gratefully acknowledge financial support from Ministry of New and Renewable Energy (MNRE), New Delhi, India (103/239/2015-NT).

References

1. S. Elena, G. Rus, J.G. Martinez, Renew. Sustainable Energy Rev. **13**(9), 2373–2384 (2009)
2. P.V. Kamat, J. Phys. Chem. C **111**(7), 2834–2860 (2007)
3. C. Yuan, H.B. Wu, Y. Xie, X.W. Lou, Angew. Chem. Int. Ed. **53**(6), 1488–1504 (2014)
4. H. Park, H.S. Jie, B. Neppolian, K. Tsujimaru, J.P. Ahn, D.Y. Lee, J.K. Park, M. Anpo, Top. Catal. **47**, 3–4 (2008)
5. B. Neppolian, Y. Hiromi, Y. Okada, H. Nishijima, M. Anpo, Catal. Lett. **105**(1), 264–271 (2005)
6. Y. Hiromi, M. Harada, J. Misaka, M. Takeuchi, B. Neppolian, M. Anpo, Catal. Today **84**, 3 (2003)
7. B. Neppolian, Q. Wang, H. Yamashita, H. Choi, Appl Catal A Gen. **333**, 2 (2007)
8. W. Ren, A. Zhihui, F. Jia, L. Zhang, X. Fan, Z. Zou, Appl Catal B: environ. **69**(15), 138–144 (2007)
9. H. Seema, K.C. Kemp, V. Chandra, K.S. Kim, Nanotechnology **23**(35), 355–705 (2012)
10. P. Mirtchev, K. Liao, E. Jaluague, Q. Qiao, Y. Tian, M. Varela, K.S. Burch, S.J. Pennycook, D.D. Perovicg, G. Ozin, J. Mater. Chem. A **2**, 8525–8533 (2014)
11. Q. Tian, W. Wu, L. Sun, S. Yang, M. Lei, J. Zhou, Y. Liu, X. Xiao, F. Ren, C. Jiang, V.A.L. Roy, A.C.S. Appl, Mater. Inter. **6**(15), 13088–13097 (2014)
12. S.G. Babu, R. Vinoth, P.S. Narayana, D. Bahnemann, B. Neppolian, APL Mater. **3**(10), 104415 (2015)
13. C. Xu, L. Cao, G. Su, W. Liu, H. Liu, Y. Yu, X. Qu, J. Hazard. Mater. **176**(1), 807–813 (2010)
14. L. Xua, H. Xua, S. Wua, X. Zhang, Appl. Surf. Sci. **258**(11), 4934–4938 (2012)
15. X. Liu, L. Cao, W. Sun, Z. Zhou, J. Yang, Res Chem Intermediat **42**(7), 6289–6300 (2016)
16. N. Li, M. Liu, Z. Zhou, J. Zhou, Y. Sun, L. Guo, Nanoscale **6**(16), 9695–9702 (2014)
17. J.J. Sen, G. Lian, Y.X. Long, G.J. Kun, J. Acta Phys. **16**(04), 312–316 (2000)
18. X. Zhang, Y. Niu, X. Meng, Y. Li, J. Zhao, CrystEngComm **15**, 8166–8172 (2013)
19. T.K. Townsend, E.M. Sabio, N.D. Browning, F.E. Osterloh, Energy Environ. Sci. **4**, 4270 (2011)
20. J.H. Kennedy, K.W. Frese, J. Electrochem. Soc. **124**, 130 (1977)
21. K.L. Hardee, A.J. Bard, J. Electrochem. Soc. **123**, 1024–1026 (1976)

22. A.G. Joly, J.R. Williams, S.A. Chambers, G. Xiong, W.P. Hess, D.M. Laman, J. Appl. Phys. **6**, 99 (2006)
23. N.J. Cherepy, D.B. Liston, J.A. Lovejoy, H.M. Deng, J.Z. Zhang, J. Phys. Chem. B **102**, 770–776 (1998)
24. A.J. Bosman, H.J. Vandaal, Adv. Phys. **19**, 1–7 (1970)
25. Q. Hua, D. Shang, W. Zhang, K. Chen, S. Chang, Y. Ma, Z. Jiang, J. Yang, W. Huang, Langmuir **27**(2), 665–671 (2011)
26. K. Sivula, R. Zboril, F.L. Formal, R. Robert, A. Weidenkaff, J. Tucek, J. Frydrych, M. Gratzel, J. Am. Chem. Soc. **132**, 7436–7444 (2010)
27. B. De, B. Voit, N. Karak, RSC Adv. **4**(102), 58453–58459 (2014)
28. Q. Hua, T. Cao, H. Bao, Z. Jiang, W. Huang, Chemsuschem **6**(10), 1966–1972 (2013)
29. C. Hao, F. Feng, X. Wang, M. Zhou, Y. Zhao, C.W. Gec, K. Wang, RSC Adv. **5**, 21161–21169 (2015)
30. S. Manoranjan, P. Biswas, Nanoscale Res. Lett. **6**(1), 441 (2011)
31. M. Guedes, J.M.F. Ferreira, A.C. Ferro, Ceram. Int. **35**(5), 1939–1945 (2009)
32. B.D. Viezbicke, S. Patel, B.E. Davis, D.P. Birnie, phys. status solidi (b) **252**(8), 1700–1710 (2015)
33. S. Norio, *Electrochemistry at metal and semiconductor electrodes* (Elsevier, Amsterdam, 1998)
34. N. Niklas, H. Fedderwitz, B. Groß, C. Noguera, J. Goniakowski, PCCP **18**(9), 6729–6733 (2016)
35. R.H. Goncalves, B.H.R. Lima, E.R. Leite, J. Am. Chem. Soc. **133**, 6012–6019 (2011)
36. J.P. Perdew, R.G. Parr, M. Levy, J.L. Balduz Jr., Phys. Rev. Lett. **49**(23), 1691 (1982)
37. Y. Xu, M.A.A. Schoonen, Am. Miner. **85**, 543–556 (2000)
38. S.K. Lakhera, A. Watts, H.Y. Hafeez, B. Neppolian, Catal. Today (2017). doi:10.1016/j.cattod.2017.03.020
39. M.S. Lundstrom, R.J. Schuelke, Solid State Electron. **25**(8), 683–691 (1982)
40. O.D. Scanlon, G.W. Watson, J. Phys. Chem. Lett. **1**, 17 (2010)
41. Y.K. Hsu, C.H. Yu, Y.C. Chen, Y.G. Lin, RSC Adv. **2–32**, 12455–12459 (2012)
42. L.C. Olsen, F.W. Addis, W. Miller, Sol. Cells **7,** 247–279 (1982–1983)